DESIGN, FABRICATION, AND CONTROL OF A HIGH-ASPECT RATIO MICROACTUATOR FOR VIBRATION SUPPRESSION IN A HARD DISK DRIVE

Kenn Oldham * **Xinghui Huang** * **Roberto Horowitz** **,[1]

* *Computer Mechanics Laboratory, University of California at Berkeley, 94720-1740* {oldham, xhhuang}@me.berkeley.edu
** *Professor of Mechanical Engineering, University of California at Berkeley, 94720-1740*
horowitz@me.berkeley.edu

Abstract: Positioning the read-write head in a hard disk drive over data bits at densities now approaching 1 terabit per square inch will novel servo configurations and controllers. This paper presents a MEMS microactuator for installation in a dual-stage servo system for a hard disk drive and controller designs that utilize the microactuator to suppress vibration of the servo arm. The microactuator uses high-aspect ratio etching and deep trench isolation to generate high force densities and good mechanical robustness. The microactuator is installed in a hard disk drive and will be used to evaluate PQ and mixed H2/H∞ controllers designed to suppress airflow-induced vibration in disk drives, currently presented with simulation results.

Keywords: Microsystems, Disk memory, Multirate control, Actuators, Vibration

1. INTRODUCTION

As storage densities in hard disk drives increase, it becomes ever more difficult to position the read-write head over shrinking magnetic bits. Conventional disk drives position the read-write head using a single large voice-coil motor (VCM) that swings the read-write head across the disk on an arm and pivot consisting of a suspension and E-block (see figure 1). Unfortunately, airflow-induced vibration of suspension and E-block resonant modes disturbs this servo arm. At very high bit densities, approaching 1 terabit per square inch, this vibration is the dominant obstacle to accurate positioning of the read-write head.

A proposed solution to this problem is to include a second-stage actuator in the servo system. Three types of dual-stage actuation have been proposed. The first is built into the suspension and moves the lower portion the slider and read-write head, typically with piezoelectric materials (Evans *et al.*, 1999) (I. Naniwa and Sato, 1999) This "actuated suspension" approach is the simplest to implement, but still faces problems of structural vibration. The second approach inserts a MEMS microactuator between the suspension and slider. This "actuated slider" method places the actuator beyond the region of structural vibration, but requires a more complicated process flow and high actuation voltages. Electrostatic (Horsley *et al.*, 1999) (White *et al.*, 2004), piezoelectric(Soeno *et al.*, 1999) (Kuwajima and Matsuoka, 2002), and electromagnetic (Tang *et al.*, 1996) actuation forces have been proposed for this configuration. The final approach places the second stage actuator in the slider itself at the read-write head (Nakamura *et al.*, 1998) (Kim and Chun, 2001). This "actuated head" arrangement gives ideal actuation location, but the integration of head, slider, and actuator fabrication is very difficult.

[1] Partially supported by Berkeley Computer Mechanics Laboratory and Information Storage Industry Consortium

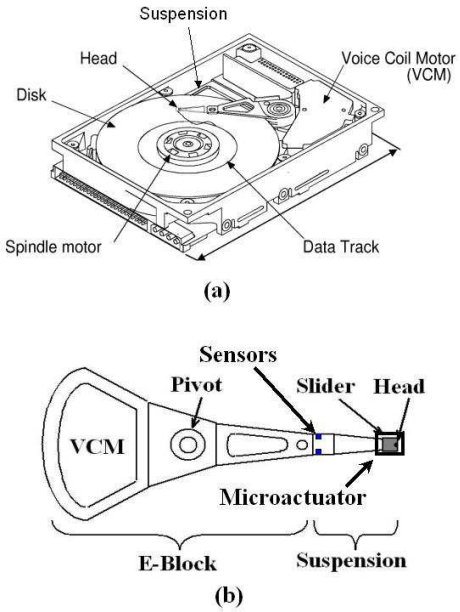

Fig. 1. Components of (a) conventional disk drive (b) dual-stage instrumented servo assembly

Servo system performance can also benefit from dedicated vibration sensing, in the form of an instrumented suspension. Such a suspension incorporates strain sensors on the suspension (see Figure 1b). These can detect vibration at higher sampling rates than may be obtained from a drive's position error signal. Optimization and fabrication of such suspensions are described in (Oldham *et al.*, 2004).

This paper focuses on an actuated-slider microactuator (hereafter referred to as the MA) and the control schemes that utilize it. The MA demonstrates advantages to force generation and mechanical properties from high-aspect ratio deep trench etching. As part of an experimental testbed for dual-stage servo control, it is compatible with a MEMS-ready protoype suspension and addresses issues often neglected by proposed actuated sliders, such as metal interconnects, robust structure for installation, and for relative position error sensing.

Using this MA, controller designs for vibration suppression based on a multirate control scheme are evaluated. MA damping and vibration control loops to suppress the MA resonant mode and suppress vibration run at a higher rate than the basic servo loop. Low-rate track-following controllers are designed for the already damped plant, using the so-called PQ method (Schroeck and Messner, 1999) or mixed H2/H∞ control via solution of linear matrix inequalities (Huang *et al.*, 2004).

2. HIGH-ASPECT RATIO MICROACTUATOR

2.1 Microactuator design

This section describes special features of the MEMS MA, especially those derived from the ability to form

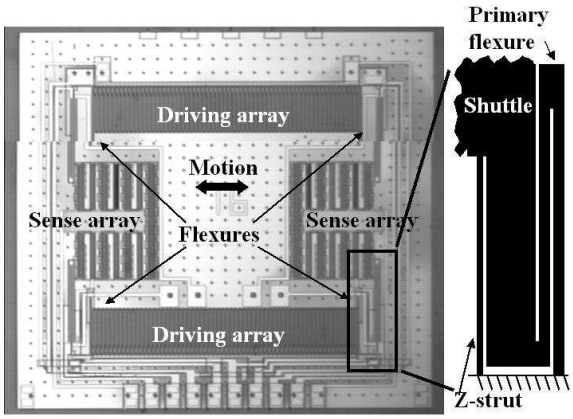

Fig. 2. Completed microactuator, flexure design inset

very high-aspect ratio structures using deep reactive-ion etching (DRIE). The MA is arranged with a central shuttle for the slider and read-write head connected at each corner by a flexure to a fixed base, as shown in Figure 2. Electrostatic driving and sensing arrays surround the moving shuttle.

High-aspect ratios in actuation The MA is driven by electrostatic gap-closing parallel-plate arrays. In parallel plate arrays, force generation is inversely proportional to the gap between plates squared, giving large forces when finger length and thickness are much larger than gap width. With DRIE, the ratio of thickness to gap width may reach 20:1, producing large forces at relatively low voltages.

Deep trench isolation DRIE trenches may be refilled with insulating material to counteract the fact that electrostatic driving force is always attractive. Two arrays are generally desired to drive a MA in either directionand to linearize the dependence of force on driving voltage. Typically, opposing parallel-plates arrays must be physically separated, requiring a large amount of space, as shown in figure 3b. Deep trench isolation allows the differential fingers to be physically connected but electrically isolated, as shown in figure 3a, increasing the number of plates that can be used for actuation.

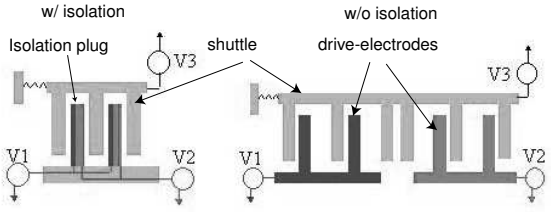

Fig. 3. Parallel plates (a) with or (b) without deep trench isolation

Deep trench isolation also simplifies the electrical operation of the device. Isolated portions of the substrates may be used to cross signals underneath surface level interconnects; only one metallization layer is required for the device. Isolated plugs may also be

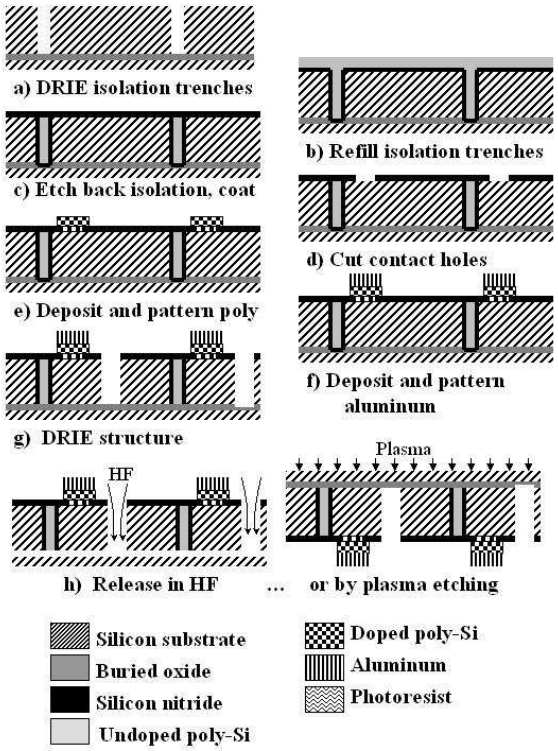

Fig. 4. Microactuator fabrication process

used as stoppers to prevent the MA shuttle shorting to stator fingers under a shock or pull-in.

Flexure design The MA also exhibits a novel compound flexure design. It is important that the MA be very compliant in the direction of desired motion but very stiff in all other directions. The least stiff secondary direction is directly out-of-plane, for which relative stiffness is controlled by the ratio of device thickness to spring width. Unfortunately, the need to carry interconnects to the read-write head limits the minimum width of the primary flexures. Instead, thin secondary struts are used to add stiffness in the out-of-plane direction, with negligible effect on in-plane compliancy, as shown in the inset of Figure 2

Relative position sensing The MA includes a capacitive sensing array for measuring the position of the shuttle relative to the MA base. The benefits of using this signal in control design were suggested in (Li and Horowitz, 2001).

2.2 Microactuator fabrication

MAs were built from silicon-on-insulator (SOI) wafers with a 100 μm device layer (refer to Figure 4. Fabrication began by forming the deep trench isolation plugs (a). Trenches were etched via DRIE, coated with silicon nitride, and refilled with undoped polysilicon (b). Silicon nitride provides good electrical isolation, but has high residual stress and is not sufficiently conformal. The undoped polysilicon refills the deep trenches more evenly. Polysilicon on the surface of the substrate was etched back to the nitride film by reactive-ion etching. The entire wafer is then coated by a second silicon nitride film (c). Contact holes through the nitride layer are etched by reactive-ion etching (d). Next, highly doped polysilicon is deposited and patterned as intereconnects, to provide a robust and adhesive base layer for metal (e). An aluminum layer is evaporated onto the substrate and patterned identically to the polysilicon(f). The silicon/aluminum stack has both high conductivity and robustness to potential damage during release of the devices. Lastly, DRIE defines the geometry of the device (g).

Table 1. Measured microactuator performance compared to predictions, before and after sidewall erosion, 15 V bias

Parameter	Units	Predicted value	Prediction after erosion	Measured value
Spring width	μm	17	15.7	15.7
Natural Frequency	Hz	2390	2470	2517
Force per Volt	$\frac{\mu N}{V}$	77	18	13
Motion per Volt, static	$\frac{\mu m}{V}$	157	34	24
Motion per Volt, 10 kHz	$\frac{\mu m}{V}$	9.5	2.4	1.4
Damping Ratio		N/A	N/A	8 %

MAs may be released from the substrate by either of two methods, as shown in Figure 4h. The simpler method is to dissolve the buried oxide layer in a wet hydroflouric acid (HF) etch. Dies are immersed in HF until individual MAs may be removed from the substrate. This is a reliable, high yield procedure, but it removes any aluminum on the device, leaving only doped polysilicon interconnects, which will reduce the quality of any signal from the capacitive sensing array. Alternatively, by etching through the SOI handle layer from the backside of the device, aluminum lines may be preserved, at the cost of additional processing steps. Backside coatings are removed and dies are bonded with photoresist face down on an encapsulated handle wafer. The dies are blanket etched back to the buried oxide by a plasma etch. Then, drops of HF etch the buried oxide and oxygen plasma scourges and/or heated photoresist stripper remove photoresist residue from the MAs.

2.3 Microactuator Performance

MAs with varying spring widths were produced by both release techniques. The dynamic response of two such MAs is shown in Fig. 5, measured by a Laser Doppler Velocimeter (LDV). The responses show single resonant modes between 1.7 and 2.2 kHz, with very clean responses to better than 20 kHz. This allows effective control of suspension vibration modes expected to appear above 4 kHz. The resonant modes are highly damping for a MEMS device, due to the large amount of squeeze-film damping between the MA's parallel plate arrays; this damping is also advantageous for control.

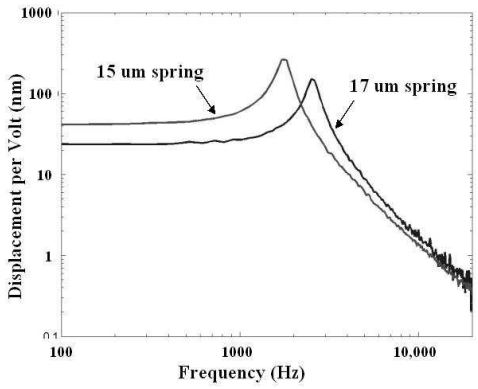

Fig. 5. Microactuator dynamic response

Force densities extracted from the LDV measurements indicate that the MAs have generate forces as large or larger than previously published results from MAs for hard disk drives. Even beyond 10 kHz, the MA is capable of producing over 1 nm displacement per volt. However, the forces are only about 15% of theoretical predictions. Table 1 lists extracted MA properties for one MA, with 17 μm springs. The discrepancy is mostly due to sidewall erosion of the DRIE trenches. Scanning electron microscope images showed trenches to be 0.5 to 1.5 μm wider than anticipated. Other factors include simplifications in our analytical spring model and imperfect installation of the slider and interconnects.

MAs have been successfully installed and flown over a spin stand at disk speeds up to 10,000 rpm. Electrical connections from suspension to metallized MAs are performed by ultrasonic wire bonding. Currently, a suspension with MA is being installed in a 3.5 inch disk drive to be used in experimental tests of MA and controller performance.

3. DUAL-STAGE MODEL WITH INSTRUMENTED SUSPENSION

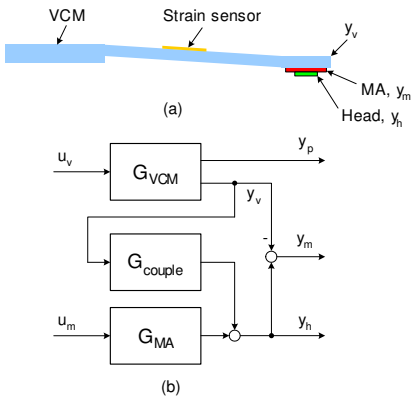

Fig. 6. (a) Schematic of the dual-stage actuator with an instrumented suspension; (b) Block diagram of the system.

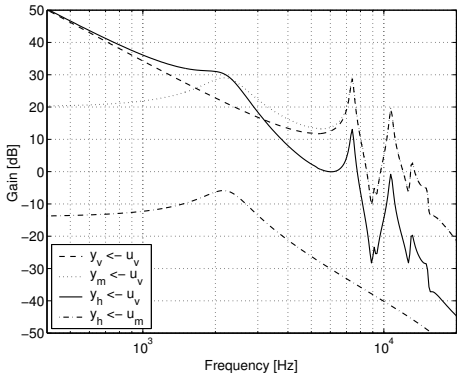

Fig. 7. Block diagram of the dual-stage actuator.

This section introduces the model of the dual-stage actuator with an instrumented suspension. Figure 6 shows the schematic and block diagram of the dual-stage actuator with an instrumented suspension, and Figure 7 shows its component frequency responses. In these figures, u_v and u_m are the control inputs to the VCM and MA respectively, y_v is the displacement of the suspension tip, y_p is the strain sensor output from the instrumented suspension, y_m is the relative motion output of the slider/head relative to the suspension tip, and y_h is the absolute head displacement, as measured by the disk's position error signal.

The transfer functions of the instrumented suspension, G_{VCM}, can be expressed as

$$G = k \sum_{i=1}^{7} \frac{r_i}{s^2 + 2\zeta_i \omega_i s + \omega_i^2}, \qquad (1)$$

where the loop gain k is a lumped gain from the current amplifier, D/A converter and position sensing, and ω_i, ζ_i and r_i are the natural frequency, damping ratio and modal constant of mode i, respectively. The first mode is the rigid body mode which cannot be detected by strain sensors. Two major suspension modes, located at 7.4 kHz and 10.7 kHz, are considered in controller design, while the full-order model, of order 7, will be used for performance analysis on the closed-loop system.

The MA can be modelled as a single mass-spring-damper system with a resonance mode around 2 kHz. Its transfer function is

$$G_{\mathrm{MA}}(s) = \frac{A_m}{s^2 + 2\zeta_m \omega_m s + \omega_m^2}, \qquad (2)$$

and its frequency response is shown in Fig. 7. Parameters for G_{MA} are $A_m = 0.2$ um/V, $\zeta_m = 0.2$, and $\omega_m = 2.25$ kHz (an MA from a different wafer than that described in the previous section). Capacitive sensing can be incorporated into the MA structure so that the relative motion output of the MA, $y_m = y_h - y_v$, is measurable.

There is coupling between the VCM and MA, that is, the VCM actuation will excite the MA dynamics through the suspension tip. However, it can be reasonably assumed that the MA actuation will not

excite the suspension dynamics due to its small moving mass. Coupling dynamics from the suspension tip displacement, y_v, to the slider motion output, y_h, can be expressed as

$$G_{\text{couple}}(s) = \frac{2\zeta_m\omega_m s + \omega_m^2}{s^2 + 2\zeta_m\omega_m s + \omega_m^2}\,. \qquad (3)$$

4. CONTROL DESIGN

4.1 MA Damping

When the relative motion output of the MA is available, active damping can be applied to the MA to have a well-behaved system and simplify the following controller design, as described in (Li and Horowitz, 2001) and (White and Hirano, 2003). The plant is first discretized at 50 kHz with a zero-order hold. Applying pole placement, the damped MA dynamics can be set to a closed-loop polynomial chosen by the designer, usually with unity damping ratio. This can be achieved by solving a Diophantine equation.

4.2 Vibration Damping and Compensation

After the MA is damped, a suspension vibration damping and compensation controller K_{in} is designed using y_p. The design of K_{in} is formulated as a standard LQG problem minimizing the following cost function

$$J = E\left\{y_h^2(k) + Ru^2(k)\right\}\,. \qquad (4)$$

The resulting control effect on the VCM is to actively damp off-track resonance modes, while the effect on the MA is to provide additional motion to compensate airflow-excited vibrations at the read/write head. Fig. 8 shows the control effect when both the MA damping and the vibration controller are closed around the plant, creating a double-input single-output (DISO) system.

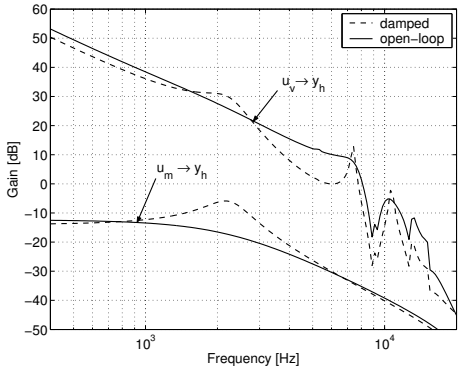

Fig. 8. Plant dynamics with/without vibration damping and compensation.

4.3 Track-following Control

After the plant is adequately damped, a low-rate track-following controller is designed for the DISO system. Two methods are explored. The first is the so-called PQ Method, reducing a controller design problem for DISO systems to two standard controller design problems for SISO systems. The first part of the PQ Method directly addresses the issue of actuator output contribution as a function of frequency, and the second part allows the use of traditional loop shaping techniques to achieve the final system performance. The second method is a multi-objective optimization method. Plant uncertainties are explicitly considered and modelled as multiplicative uncertainties at the inputs u_v and u_m. Tracking performance optimization can be expressed as the minimization of the H_2 norm of the general plant including all disturbances and track runout models. Robust stability is guaranteed by satisfying linear matrix inequality constraints. The reader is referred to (Schroeck and Messner, 1999) and (Huang *et al.*, 2004) for more details about the two designs.

5. DESIGN RESULTS

5.1 Simulation

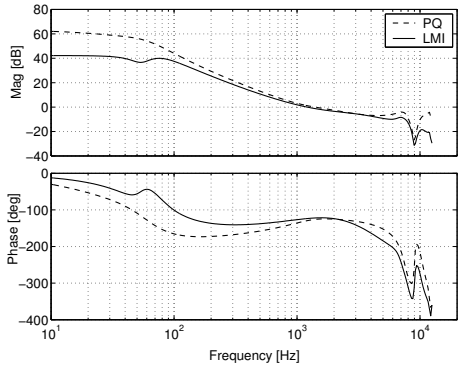

Fig. 9. PQ plots for the two designs.

Fig. 9 shows the PQ plots for the two designs. The PQ value is defined as the ratio between the two channels: $G_{\text{PQ}} := G_{\text{VCM}}/G_{\text{MA}}$, where G_{VCM} and G_{MA} are the open-loop transfer functions from the PES to y_h via VCM and MA respectively. Its gain margin indicates the interference situation between the two actuators. We see that for both systems the hand off frequencies are around 1.4 kHz. At this frequency, both curves have large phase margins of about 55 degrees, implying little destructive interference.

Fig. 10 shows the closed-loop sensitivity responses of the two designs. The closed-loop servo bandwidth is 2.2 kHz for the PQ design and 3 kHz for the LMI design. The PQ design has more error rejection in the low-frequency range; the LMI design expands the error suppression region to a higher frequency.

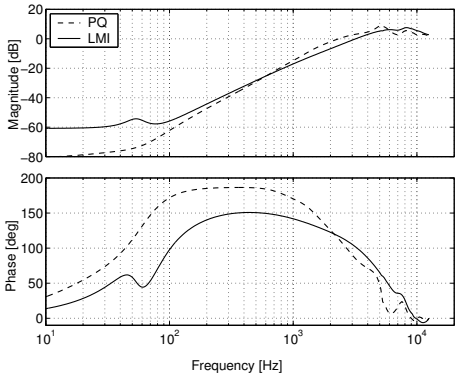

Fig. 10. Closed-loop sensitivity responses of the two designs.

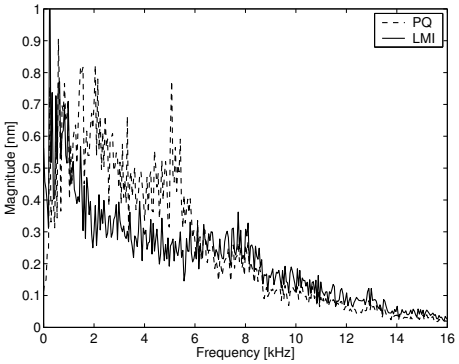

Fig. 11. Power spectrum densities of the position error signals of the two designs.

Finally, time-domain simulation is conducted and the spectra of PES are shown in Fig. 11. In the simulation, track runout, airflow disturbances and measurement noises are injected into the plant. As shown, airflow-excited suspension vibrations have been effectively suppressed. The final RMS value of PES is 4.8 nm for the PQ design, and 3.8 nm for the LMI design.

5.2 Experimental results

A suspension with MEMS MA is currently being installed in a hard disk drive in order to verify controller performance experimentally. Experimental results are anticipated in the upcoming year, and will be compared to the simulation results above.

6. CONCLUSION

A robust, high force microactuator has been fabricated and included in several novel dual-stage control schemes for hard disk drives. The microactuator utilizes high-aspect ratio trenches and deep trench isolation to form a compact electrostatic parallel-plate array. This produces very large electrostatic forces, though performance was limited by imperfect processing of the deep trenches. The microactuator demonstrates a very clean dynamic response, with especially good gains at high frequencies. Multi-rate controllers are presented to capitalize on the microactuator presence. In simulation, the system achieves a RMS position error of 4.8 nm with a PQ controller or 3.8 nm with an LMI design. Experimental verification is anticipated in the near future.

REFERENCES

Evans, R.B., J.S. Griesbach and W.C. Messner (1999). Piezoelectric microactuator for dual-stage control. *IEEE Trans. on Magn.* **35**, 977–81.

Horsley, D., N. Wongkomet, R. Horowitz and A. Pisano (1999). Precision positioning using a microfabricated electrostatic actuator. *IEEE Transactions on Magnetics* **35**, 993–999.

Huang, X., R. Nagamune, R. Horowitz and Y. Li (2004). Design and analysis of a dual-stage disk drive servo system using an instrumented suspension. In: *Proc. of Amer. Control Conf.*. Vol. 4. pp. 535–540.

I. Naniwa, S. Nakamura, S. Saegusa and K. Sato (1999). Low voltage driven piggy-back actuator of hard disk drives. *IEEE International MEMS 99 Conference* pp. 49–52.

Kim, B.-H. and K. Chun (2001). Fabrication of an electrostatic track-following micro actuator for hard disk drives using soi wafer. *Journal of Micromechanics and Microengineering*.

Kuwajima, H. and K. Matsuoka (2002). Thin film piezoelectric dual-stage actuator for hdd. *InterMag Europe, Session BS04* pp. 229–236.

Li, Y. and R. Horowitz (2001). Mechatronics of electrostatic microactuators for computer disk drive dual-stage servo systems. *IEEE/ASME Trans. Mechatronics* **6**(2), 111–121.

Nakamura, S., K. Suzuki, M. Ataka and H. Fujita (1998). An electrostatic microactuator for a magnetic head tracking system of hard disk drives. *Advances in Info. Storage Systems* **10**, 83–99.

Oldham, K., S. Kon and R. Horowitz (2004). Fabrication and optimal strain sensor placement in an instrumented disk drive suspension for vibration suppression. *Proc. Amer. Control Conf.*

Schroeck, S.J. and W.C. Messner (1999). On controller design for linear time-invariant dual-input single-output systems. *Proc. Amer. Control. Conf.* pp. 4122–4126.

Soeno, Y., S. Ichikawa, T. Tsuna, Y. Sato and I. Sato (1999). Piezoelectric piggy-back microactuator for hdd. *IEEE Trans. Mag.* **35**(2), 983–987.

Tang, W., V. Temesvary, J.J. Yao, Y.-C. Tai and D.K. Miu (1996). Silicon microactuators for computer disk drives. *Japaneses J. Appl. Physics*.

White, M., T. Hirano, H. Yang, K. Scott, S. Pattanaik and F.-Y. Huang (2004). High bandwidth hard disk drive tracking using a moving-slider mems microactuator. *8th IEEE Int'l Workshop Advanced Motion Control* pp. 299–304.

White, M.T. and T. Hirano (2003). Use of relative position signal for microactuators in hard disk drives. *Proc. Amer. Control Conf.* **3**, 2535–2540.